



Evaluation of a High Resolution Wind Model Over a Complex Terrain Surface

**by Sam S. Chang, Dennis M. Garvey,
Chatt C. Williamson, and Giap Huynh**

ARL-TR-4773

April 2009

NOTICES

Disclaimers

The findings in this report are not to be construed as an official Department of the Army position unless so designated by other authorized documents.

Citation of manufacturer's or trade names does not constitute an official endorsement or approval of the use thereof.

Destroy this report when it is no longer needed. Do not return it to the originator.

Army Research Laboratory

Adelphi, MD 20783-1197

ARL-TR-4773**April 2009**

Evaluation of a High Resolution Wind Model Over a Complex Terrain Surface

**Sam S. Chang, Dennis M. Garvey
Chatt C. Williamson, and Giap Huynh
Computational and Information Sciences Directorate, ARL**

REPORT DOCUMENTATION PAGE				Form Approved OMB No. 0704-0188	
<p>Public reporting burden for this collection of information is estimated to average 1 hour per response, including the time for reviewing instructions, searching existing data sources, gathering and maintaining the data needed, and completing and reviewing the collection information. Send comments regarding this burden estimate or any other aspect of this collection of information, including suggestions for reducing the burden, to Department of Defense, Washington Headquarters Services, Directorate for Information Operations and Reports (0704-0188), 1215 Jefferson Davis Highway, Suite 1204, Arlington, VA 22202-4302. Respondents should be aware that notwithstanding any other provision of law, no person shall be subject to any penalty for failing to comply with a collection of information if it does not display a currently valid OMB control number.</p> <p>PLEASE DO NOT RETURN YOUR FORM TO THE ABOVE ADDRESS.</p>					
1. REPORT DATE (DD-MM-YYYY)		2. REPORT TYPE		3. DATES COVERED (From - To)	
April 2009		Final			
4. TITLE AND SUBTITLE Evaluation of a High Resolution Wind Model Over a Complex Terrain Surface				5a. CONTRACT NUMBER	
				5b. GRANT NUMBER	
				5c. PROGRAM ELEMENT NUMBER	
6. AUTHOR(S) Sam S. Chang, Dennis M. Garvey, Chatt C. Williamson, and Giap Huynh				5d. PROJECT NUMBER	
				5e. TASK NUMBER	
				5f. WORK UNIT NUMBER	
7. PERFORMING ORGANIZATION NAME(S) AND ADDRESS(ES) U.S. Army Research Laboratory ATTN: AMSRD-ARL-CI-ED 2800 Powder Mill Road Adelphi, MD 20783-1197				8. PERFORMING ORGANIZATION REPORT NUMBER ARL-TR-4773	
9. SPONSORING/MONITORING AGENCY NAME(S) AND ADDRESS(ES)				10. SPONSOR/MONITOR'S ACRONYM(S)	
				11. SPONSOR/MONITOR'S REPORT NUMBER(S)	
12. DISTRIBUTION/AVAILABILITY STATEMENT Approved for public release; distribution unlimited.					
13. SUPPLEMENTARY NOTES					
14. ABSTRACT A complete and comprehensive description of the high resolution wind (HRW) model is presented. The HRW model has been in development at the U.S. Army Research Laboratory, formerly U.S. Army Atmospheric Sciences Laboratory, since 1978. This model is a two-dimensional, diagnostic atmospheric surface-layer wind model with a horizontal grid spacing of the order of 100 m over a domain of about 5 by 5 km. It uses Gauss' principle of least constraint and a direct variational relaxation method to adjust an initially uniform wind field to conform with topography, mass conservation, and buoyancy forces. A distinctive feature of the model is the use of a non-orthogonal, terrain following, warped coordinate system. A valuable observational dataset of surface wind has been provided from the field study of Meteorology and Diffusion Over Non-Uniform Areas (MADONA) at Porton Down, Salisbury, England during September and October 1992. Using the MADONA data, a critical evaluation for the HRW model for 39 cases has been carried out. The results of this study are presented, indicating both the range of validity and the limitations of the HRW model.					
15. SUBJECT TERMS High resolution wind (HRW) model, atmospheric surface layer					
16. SECURITY CLASSIFICATION OF:			17. LIMITATION OF ABSTRACT UU	18. NUMBER OF PAGES 45	19a. NAME OF RESPONSIBLE PERSON Sam S. Chang
a. REPORT Unclassified	b. ABSTRACT Unclassified	c. THIS PAGE Unclassified			19b. TELEPHONE NUMBER (Include area code) (301) 394-1988

Contents

List of Figures	iv
List of Tables	iv
Acknowledgments	v
1. Introduction	1
2. Description of the HRW Model	2
2.1 Gauss's Principle of Least Constraint	2
2.2 Warped Coordinate System.....	4
2.3 Empirical Surface Layer Profiles	9
2.4 Computational Aspects and Algorithm	11
2.4.1 Data Input and Model Setup.....	12
2.4.2 Relaxation Scheme	14
2.4.3 Data Output	15
3. Results of the Model Evaluation	16
3.1 The MADONA Data	16
3.2 The Model Simulations	17
3.3 The Results of Linear Regression Analysis	19
3.4 Discussion	28
4. Conclusions	30
5. References	32
Distribution List	34

List of Figures

Figure 1. The terrain following, warped and non-orthogonal coordinate system with three base vectors (\vec{a}_1 , \vec{a}_2 , and \vec{a}_3) which is defined by equations 11, 12, and 13, respectively. \vec{V} is a wind vector. A computational volume element with top (HMNP) and bottom (OEFG, shaded) is also shown, see text for details.	5
Figure 2. Computational flow chart for the HRW model. This chart illustrates the three essential stages and their major routines.	12
Figure 3. Locations of MADONA measurements sites (M1 through M15) plotted on terrain contours.	17
Figure 4a. Scatter diagrams for simulated wind direction (y , degree) versus observed values (x , degree). The straight lines result from the linear regression analysis, equation 42.	20
Figure 4b. Scatter diagrams for simulated wind speed (y , ms^{-1}) versus observed values (x , ms^{-1}). The straight lines result from the linear regression analysis, equation 42.	21
Figure 5. Same as figure 4a except for three wind direction categories as defined by equation 43a, b, c.	24
Figure 6. Same as figure 4b except for three-wind speed categories as defined, by equation 43d, e, f.	25
Figure 7. Same as figure 4 except for three stability categories as defined by equation 44a, b, c.	27

List of Tables

Table 1. A list of input and output data for the HRW model.	13
Table 2. The 39 cases for the HRW simulations. ΔQ is defined by equation 24a in the text.	18
Table 3. The value of n (data pair number), a (slope), b (intercept), r (correlation coefficient), and S (standard deviation) from the linear regression equation 42, for wind direction and wind speed, respectively.	22
Table 4. Same as table 3 except for three wind direction categories as defined by equation 43 (a, b, c) and three wind speed categories as defined by equation 43 (d, e, f).	23
Table 5. Same as table 3 except for three atmospheric stability categories defined by equation 44a, b, c.	28

Acknowledgments

We appreciate Mr. Ronald Cionco, our now retired colleague, who played a leading role in the early development of the model, and continued development and application of the model for various scenarios. Dr. Jon Mercurio, also retired colleague, contributed to the construction of the model and this manuscript. Dr. James Cogan and Dr. Douglas Brown offered administrative support for this technical report.

Miss Patricia Cordes, a student at the Academy of the Holy Cross, who participated in the Science and Engineering Apprentice Program sponsored by the U.S. Army Research Laboratory in Summer 1999, contributed much of the linear regression analysis and graphing. Mr. John Byers helped check the data files used in this study. Mr. Ron Meyers provided useful discussions on the model. Mr. Richard Hasenauer helped with the figures. Ms. Deborah Lehtinen has typed the manuscript with great skill.

INTENTIONALLY LEFT BLANK

1. Introduction

During the last three decades meteorological researchers at the U.S. Army Research Laboratory (ARL), formerly the Atmospheric Sciences Laboratory (ASL), have conceived, developed, and used a high resolution wind (HRW) model. The HRW model is a micro-alpha scale (Orlanski, 1975), two-dimensional, diagnostic model that simulates wind and temperature fields in the atmospheric surface layer, taking into account both complex terrain topography and thermal structure over a limited area. The computational domain size can range from a 2 km square to a 20 km square with grid resolutions varying from 40 m to 400 m, respectively. The vertical thickness of the computational layer is designed to be one tenth the magnitude of the grid size. A typical grid size of 100 m, therefore, produces simulated fields at a level 10 m above the surface.

The HRW model was originally formulated by Ball and Johnson (1978) who described its theoretical basis and computational structure in a technical report submitted to ASL. This geographically re-locatable model was designed to be incorporated in the U.S. Army Experimental Prototype Automatic Meteorological System for the estimation of the surface layer wind field at sub-mesoscale resolution over a limited area in broken topography. Later the HRW model was further developed as a stand-alone model, as well as an integral component of a hierarchy of nested meso- and micro-meteorological models (Cionco, 1987). A distinctive feature of the HRW model is that it has adopted a warped coordinate system to address the intimate interaction between the surface layer and the variable ground features. As far as the authors are aware, this approach is unique; virtually no meso- or micro-scale models have been formulated with this approach. The HRW model has been tested and used for a variety of applications, e.g., Weber et al. (1995), Thykier-Nielsen et al. (1995), Cionco and Byers (1995, 1997), Cionco (1998), Cionco et al. (1998), Cionco and Ellefsen (1998). Although the model has been tested and used for a long time, it has not been thoroughly evaluated due to the fact that adequate observational data at a resolution of 100 m or so are extremely scarce. Fortunately, the multinational, high-resolution field study of Meteorology and Diffusion over Non-Uniform Areas (MADONA) during September and October 1992 has provided a valuable observational dataset. Cionco et al. (1999) have given a comprehensive description of the MADONA project, including the dataset. The MADONA field study was designed and conducted for, among other purposes, high-resolution meteorological data collection in an effort to obtain terrain-influenced meteorological data. Thirty-one days of meteorological data were collected. High-resolution and standard micro-scale, boundary layer, and synoptic meteorological sensors including 15 wind speed/direction sets were deployed over the MADONA topography (a 9 km by 7.5 km area). This well-documented database is suitable and valuable for the evaluation and validation of the HRW model.

The objectives of this report are twofold. The first objective is to provide a concise description of the HRW model as systematically and completely as possible. The lengthy paper by Ball and Johnson (1978) was not published in the open literature and is not readily available for interested readers. A limited number of papers presented in a book (Cionco, 1985) or at conferences (cited above) have separately described only gross features of the model without providing necessary details. Section 2 provides the basic theory, warped coordinate system, mathematical formulation, and the computational algorithms of the model. The second objective is to present the results of a critical evaluation of the model using the MADONA database (section 3). Finally, the last section (section 4) gives conclusions from the present study of the HRW model, and relates these results to a companion evaluation of the model in a report by Williamson et al. (2005).

2. Description of the HRW Model

2.1 Gauss's Principle of Least Constraint

The HRW model uses Gauss's principle of least constraint directly rather than the more commonly employed Newton's laws of motion. A discussion of this principle applied to systems of point particles can be found in Lanczos (1966). As applied to non-viscous, incompressible fluids, the principle can be expressed as

$$\delta \left[\iiint \frac{1}{2} \rho (\vec{A} + \vec{g})^2 d\tau + \iint p \vec{A} \cdot d\vec{\sigma} \right] = 0 \quad , \quad (1)$$

where δ denotes a variation of the two integrals in square brackets. The vector \vec{A} is the acceleration, $d\vec{V}/dt$, where \vec{V} is the velocity vector; and $-\vec{g}$ is the acceleration of gravity, the only external force considered. The two integrals above are over a material volume (τ) and its boundary surface (σ), respectively. The symbols ρ and p are the fluid density and pressure respectively. For the atmosphere, ρ and p are related by the equation of state for an ideal gas,

$$p = \rho RT, \quad (2)$$

where R is the specific gas constant for air, and T is the absolute temperature. The more conservative potential temperature θ is related to T as

$$\theta = T \left(p_{ref} / p \right)^{R/c_p}, \quad (3)$$

where p_{ref} is the reference pressure taken as 100 kPa and c_p is the specific heat at constant pressure.

Equating the variation of the expression in brackets to zero implies that the air motion takes place in such a way as to minimize constraint forces arising solely from kinematic conditions. In

this case the constraints are the boundary conditions and conservation of mass, which for an incompressible fluid is expressed as

$$\nabla \cdot \vec{V} = 0. \quad (4)$$

This constraint results in the pressure gradient acting as a force of constraint necessary to enforce incompressibility. Ball and Johnson (1978) discuss this result in greater detail.

In order to account for atmospheric thermal effects, additional assumptions are needed. First, the variables in the equation of state are decomposed as

$$\rho = \rho_0 + \rho', p = p_0 + p', T = T_0 + T', \theta = \theta_0 + \theta', \quad (5)$$

where the variables with zero subscripts denote ambient or mean values while the same variables with primes represent departures from the ambient. Secondly, using the Boussinesq approximation, equation 1 can be approximated by

$$\delta \left[\iiint \frac{1}{2} \rho_0 (\vec{A} + b \vec{g})^2 d\tau + \iint p' \vec{A} \cdot d\vec{\sigma} \right] = 0 \quad (6)$$

$$b = (\rho' / \rho_0) = (-\theta' / \theta_0), \quad (6a)$$

where $-b \vec{g}$, the effective external acceleration, is the buoyancy acceleration, and b is the buoyancy parameter defined by equation 6a. A detailed discussion of the Boussinesq approximation is provided by, e.g., Stull (1988, Chapter 3). Likewise the effective pressure in equation 6 is the fluctuating pressure (p'), the departure from the ambient pressure (p_0). It is assumed that both p' and p_0 satisfy the hydrostatic equation

$$dp_0 = -\rho_0 g dz, \quad dp' = -\rho' g dz, \quad (7)$$

where z denotes vertical height. Thirdly, similar to equation 6 a variational expression can be applied to the potential temperature field

$$\delta \left[\iiint \frac{1}{2} \left(\frac{d\theta}{dt} \right)^2 d\tau \right] = 0, \quad (8a)$$

where the adiabatic condition has been assumed. Equation 8a implies that

$$\frac{d\theta}{dt} = \frac{\partial \theta}{\partial t} + \vec{V} \cdot \nabla \theta = 0. \quad (8b)$$

For a steady state, equation 8a is equivalent to

$$\delta \left[\iiint \left\{ \nabla \cdot (\theta \vec{V}) \right\}^2 d\tau \right] = 0. \quad (8c)$$

This equation is needed in order to make the temperature field and the buoyancy forces consistent with the wind field.

For the application of the basic variational principles, equations 6 and 8c, to a single surface layer, further simplification is required. This single surface layer is of constant thickness in a direction normal to the terrain surface and follows the warped ground surface. The second (surface) integral in equation 6 contains the pressure fluctuation p' . This p' term is extremely difficult to estimate. A practical alternative is to reformulate equation 6. With the help of Gauss's theorem, equation 6 can be rewritten for the single surface layer as

$$\delta \left[\iiint \left\{ \frac{1}{2} \rho_0 \left(\vec{A}_s + \vec{A}_n + b \vec{g}_s + b \vec{g}_n \right)^2 + \nabla \cdot p' \left(\vec{A}_s + \vec{A}_n \right) \right\} d\tau \right] = 0,$$

where the subscripts s and n denote the surface parallel and surface normal component, respectively. The integrand in the above equation can be rewritten as

$$\frac{1}{2} \rho_0 \left[\left(\vec{A}_s + \vec{A}_n + b \vec{g}_s \right)^2 + \left(b \vec{g}_n \right)^2 + 2b \vec{A}_n \cdot \vec{g}_n \right] + \nabla \cdot p' \vec{A}_n + \nabla \cdot p' \vec{A}_s$$

One part of the second-to-last term in the above expression, $(\nabla \cdot p' \vec{A}_n)$ can be used to cancel the last term within the brackets, $(\rho_0 b \vec{A}_n \cdot \vec{g}_n)$ since $\partial p' / \partial n = -\rho' g_n$ as implied by equation 7. The absence of the cross product of \vec{A}_n and $b \vec{g}_n$ suggests that $b \vec{g}_n$ may be ignored. The other part of the second-to-last term, $(p' \nabla \cdot \vec{A}_n)$ as well as the last term, $(\nabla \cdot p' \vec{A}_s)$ can be neglected because p' is usually small. Consequently equation 6 is further simplified as

$$\delta \left[\iiint \left(\vec{A} + b \vec{g}_s \right)^2 d\tau \right] = 0 \quad (9)$$

where only the surface parallel component of buoyancy $b \vec{g}_s$ remains, and the multiplicative constant $(\rho_0/2)$ has been neglected. The surface parallel simplification in equation 9 assumes that for the surface layer the acceleration normal to the terrain surface is not affected by the normal buoyancy force $(b \vec{g}_n)$.

2.2 Warped Coordinate System

A terrain-following, warped, non-orthogonal coordinate system is employed in the HRW model in order to account for a complex and varying terrain surface as accurately as possible. Figure 1 is a diagram of the warped coordinate system. The upper portion of figure 1 indicates a Cartesian coordinate system with respect to a horizontal reference plane in which \vec{i} , \vec{j} , and \vec{k} are three unit vectors along the three orthogonal directions (x , y , and z), respectively. Any position on the terrain surface is given by the vector

$$\vec{r} = x \vec{i} + y \vec{j} + h(x, y) \vec{k}, \quad (10)$$

where $h(x, y)$ is the surface elevation.

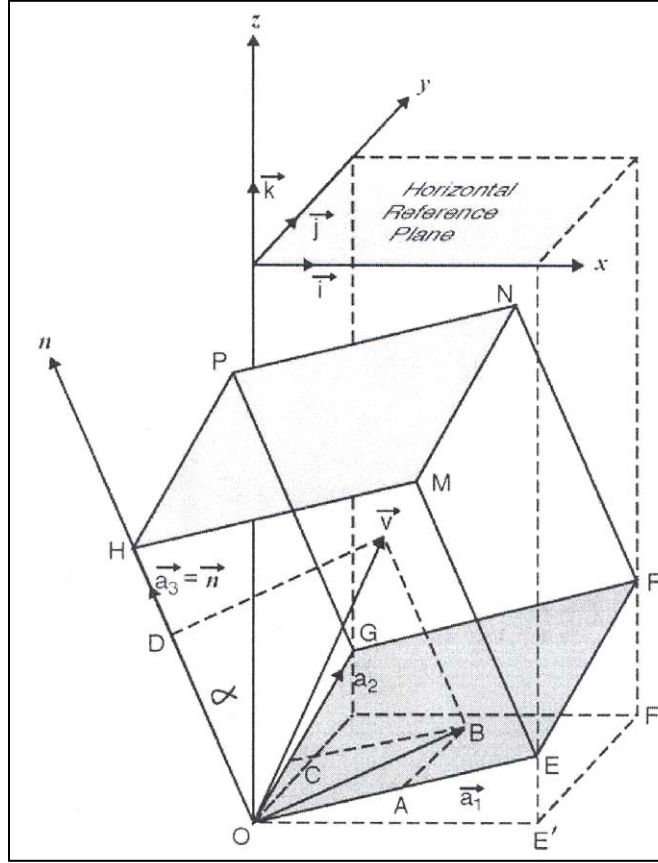


Figure 1. The terrain following, warped and non-orthogonal coordinate system with three base vectors (\vec{a}_1 , \vec{a}_2 , and \vec{a}_3) which is defined by equations 11, 12, and 13, respectively. \vec{V} is a wind vector. A computational volume element with top (HMNP) and bottom (OEFG, shaded) is also shown, see text for details.

The lower portion of figure 1 shows three base vectors, which are defined by

$$\vec{a}_1 = \frac{\partial \vec{r}}{\partial x} = \vec{i} + h_x \vec{k}, \quad h_x = \frac{\partial h}{\partial x}, \quad a_1 = |\vec{a}_1| = \sqrt{1 + h_x^2} \quad (11)$$

$$\vec{a}_2 = \frac{\partial \vec{r}}{\partial y} = \vec{j} + h_y \vec{k}, \quad h_y = \frac{\partial h}{\partial y}, \quad a_2 = |\vec{a}_2| = \sqrt{1 + h_y^2} \quad (12)$$

$$\vec{a}_3 = \vec{n} = \frac{1}{\sqrt{a}} (-h_x \vec{i} - h_y \vec{j} + \vec{k}), \quad a = 1 + h_x^2 + h_y^2, \quad |\vec{a}_3| = 1. \quad (13)$$

These three vectors \vec{a}_1 , \vec{a}_2 , and \vec{a}_3 establish a warped coordinate system. Notice that \vec{a}_1 and \vec{a}_2 are parallel to the surface, but are not unit vectors. The vectors \vec{a}_1 and \vec{a}_2 are not perpendicular to each other, and hence, the warped coordinate system is not an orthogonal coordinate system.

The vector \vec{a}_3 is a unit vector and is perpendicular to the terrain surface (\vec{a}_1 and \vec{a}_2). The volume of the parallelepiped formed by these three base vectors is

$$\vec{a}_1 \cdot (\vec{a}_2 \times \vec{a}_3) = \sqrt{a}. \quad (14)$$

The angle between \vec{a}_3 and the vertical z axis is α as indicated in figure 1,

$$\cos \alpha = 1/\sqrt{a}. \quad (15)$$

It is useful to define the system of reciprocal base vectors denoted by a superscript

$$\vec{a}^1 = (\vec{a}_2 \times \vec{a}_3) / \sqrt{a} = \frac{1}{a} \left[(1 + h_y^2) \vec{i} - h_x h_y \vec{j} + h_x \vec{k} \right] \quad (16)$$

$$\vec{a}^2 = (\vec{a}_3 \times \vec{a}_1) / \sqrt{a} = \frac{1}{a} \left[-h_x h_y \vec{i} + (1 + h_x^2) \vec{j} + h_y \vec{k} \right] \quad (17)$$

$$\vec{a}^3 = (\vec{a}_1 \times \vec{a}_2) / \sqrt{a} = \frac{1}{\sqrt{a}} \left[-h_x \vec{i} - h_y \vec{j} + \vec{k} \right] = \vec{a}_3. \quad (18)$$

The reciprocal vector \vec{a}^3 is identical with \vec{a}_3 or \vec{n} , the unit vector normal to the terrain surface. The reciprocal vectors \vec{a}^1 and \vec{a}^2 are parallel to the surface, but distinct from \vec{a}_1 and \vec{a}_2 . Also \vec{a}^1 and \vec{a}^2 are not perpendicular to each other. The system of reciprocal vectors facilitates operations because

$$\vec{a}_r \cdot \vec{a}^s = \delta_{rs} \quad r, s = 1, 2, 3, \quad (19)$$

where $\delta_{rs} = 1$ if $s = r$, and $\delta_{rs} = 0$ otherwise.

A three-dimensional wind velocity vector in the atmospheric surface layer can be expressed as

$$\vec{V} = V^1 \vec{a}_1 + V^2 \vec{a}_2 + V^3 \vec{a}_3 = V^i \vec{a}_i. \quad (20)$$

where $V^1 \vec{a}_1 = \vec{OA}$, $V^2 \vec{a}_2 = \vec{OC}$, and $V^3 \vec{a}_3 = \vec{OD}$ as illustrated in figure 1. The vector \vec{OB} is the component of the wind velocity along the terrain surface. The sum convention for repeated index (i) is used in equation 20 and hereafter. Notice that $(V)^2 \neq (V^1)^2 + (V^2)^2 + (V^3)^2$ due to non-orthogonality of the coordinates. The component V^3 is called the surface normal velocity component or the impaction vertical motion. Note that V^3 is not the vertical velocity (w) in terms of a Cartesian coordinate system. It is not difficult to prove that

$$V^1 = \frac{1}{a} \left[(1 + h_y^2) u - h_x h_y v + h_x w \right] \quad (21a)$$

$$V^2 = \frac{1}{a} \left[-h_x h_y u + (1 + h_x^2) v + h_y w \right] \quad (21b)$$

$$V^3 = \frac{1}{\sqrt{a}} \left[-h_x u - h_y v + w \right] \quad (21c)$$

where u and v are the wind velocity components along x and y direction, respectively (figure 1). The surface kinematic boundary condition is usually expressed by

$$w(z = h) = \vec{V} \cdot \nabla h(x, y) \quad (22a)$$

with the help of equation 21c, the above condition leads to

$$V^3(z = h) = 0 \quad (22b)$$

That means the surface kinematic condition imposes zero impaction vertical motion, but not the Cartesian vertical velocity (w) at the terrain surface. As shown in figure 1, the acceleration of gravity is

$$-\vec{g} = -g\vec{k} = -g \left(\cos \alpha \cdot \vec{n} + \sin \alpha \cdot \vec{S} \right) = -\left(\vec{g}_n + \vec{g}_s \right) \quad (23)$$

where $-\vec{g}_n$ and $-\vec{g}_s$ denote the surface normal and surface parallel component of $-\vec{g}$, respectively. The term \vec{S} is a unit vector along the \vec{OB} direction in figure 1. As discussed earlier, $b\vec{g}_s$ is used for the calculation of buoyancy acceleration in equation 9. Besides the buoyancy parameter (b), a surface heating (dq) is introduced in the model. From the First Law of thermodynamics for an ideal gas, the heating can be written as

$$dq = c_p dT - dp/\rho = c_p T(d\theta/\theta)$$

where the definition of θ , equation 3, has been used, see, e.g., Wallace and Hobbs (1977). Hence for the surface layer, dq can be related to the buoyancy parameter (b) as defined by equation 6a

$$dq = c_p T_{sfc} \left[\frac{\theta_{sfc} - \theta_0}{\theta_0} \right] = -c_p T_{sfc} b, \quad (24)$$

where the subscript “sfc” denotes the surface layer. In order to evaluate the integrals of equations 8c and 9, we use a computational volume element for the single surface layer as sketched in figure 1. This volume element, also called local flux box, consists of the layer between the terrain surface, (h) and a constant normal height (d) with lateral lengths ℓ_1 and ℓ_2 as indicated in figure 1

$$\ell_1 = OE = GF = la_1 = l\sqrt{1+h_x^2} \quad (25a)$$

$$\ell_2 = OG = EF = la_2 = l\sqrt{1+h_y^2}. \quad (25b)$$

where $l = OE' = E'F'$ is the side length of the square which is the projection of the volume element on the horizontal reference plane. The volume element is not rectangular and its volume ($\Delta\tau$) is

$$\Delta\tau = (l_1/a_1)\vec{a}_1 \cdot \left[(l_2/a_2)\vec{a}_2 \times d\vec{a}_3 \right] = l^2 d\sqrt{a}. \quad (26)$$

For reference, the lateral faces of the local flux box are numbered counterclockwise (1), (2), (3), and (4) as shown by EFNM, FGPN, GOHP, and OEMH, and (5) and (6) denote top (HMNP) and bottom (OEFG) faces, respectively in figure 1. The vector expressions of the six surface areas are

$$\vec{\Delta S}_1 = \left[(l_2/a_2)\vec{a}_2 \times d\vec{a}_3 \right]_1 = ld \left[\sqrt{a}\vec{a}^1 \right]_1 \quad (27a)$$

$$\vec{\Delta S}_2 = \left[d\vec{a}_3 \times (l_1/a_1)\vec{a}_1 \right]_2 = ld \left[\sqrt{a}\vec{a}^2 \right]_2 \quad (27b)$$

$$\vec{\Delta S}_3 = - \left[(l_2/a_2)\vec{a}_2 \times d\vec{a}_3 \right]_3 = -ld \left[\sqrt{a}\vec{a}^1 \right]_3 \quad (27c)$$

$$\vec{\Delta S}_4 = - \left[d\vec{a}_3 \times (l_1/a_1)\vec{a}_1 \right]_4 = -ld \left[\sqrt{a}\vec{a}^2 \right]_4 \quad (27d)$$

$$\vec{\Delta S}_5 = \left[(l_1/a_1)\vec{a}_1 \times (l_2/a_2)\vec{a}_2 \right]_5 = l^2 \left[\sqrt{a}\vec{a}^3 \right]_5 \quad (27e)$$

$$\vec{\Delta S}_6 = - \left[(l_1/a_1)\vec{a}_1 \times (l_2/a_2)\vec{a}_2 \right]_6 = -l^2 \left[\sqrt{a}\vec{a}^3 \right]_6, \quad (27f)$$

where \vec{a}^1, \vec{a}^2 , and \vec{a}^3 have been defined by equations 16, 17, and 18 respectively. The subscripts: (1 through 6) in equation 27 mean that all terrain dependent quantities must be evaluated using representative (average) values on that surface. The surface area vector $\vec{\Delta S}_k$ ($k=1, \dots, 6$) is in the outward normal direction of each face. Using the divergence theorem for the volume element, the condition of mass conservation equation 4 can be approximated by

$$\nabla \cdot \vec{V} = \frac{1}{\Delta\tau} \sum_k (\vec{V} \cdot \vec{\Delta S})_k = \frac{1}{\Delta\tau} \sum_k \left[(V^1\vec{a}_1 + V^2\vec{a}_2 + V^3\vec{a}_3) \cdot \vec{\Delta S} \right]_k = 0. \quad (28a)$$

From equations 19 and 27 the above condition yields

$$\left(\sqrt{a}V^3 \right)_5 - \left(\sqrt{a}V^3 \right)_6 = -\frac{d}{l} \left[\left(\sqrt{a}V^1 \right)_1 + \left(\sqrt{a}V^2 \right)_2 - \left(\sqrt{a}V^1 \right)_3 - \left(\sqrt{a}V^2 \right)_4 \right] = \frac{d}{l} W, \quad (28b)$$

where W is only a notation to be used later. The term $(\sqrt{a}V^3)_6$ in equation 28b vanishes due to equation 22b. The surface normal velocity (V^3) in the surface layer is of order $(d/l) < 0.1$ with respect to surface parallel components (V^1 and V^2 term) as implied by equation 28. Using

equations 19, 20, and 27, and dyadic (tensor) analysis (Tai, 1992, for example) the acceleration vector for the local flux box can be written as

$$\begin{aligned}
\vec{A} &= \nabla \cdot (\vec{V}\vec{V}) = \nabla \cdot (\vec{V}^i \vec{V}^j \vec{a}_i \vec{a}_j) = \frac{1}{\Delta \tau} \sum_k \left[(\vec{V}^i \vec{V}^j \vec{a}_i \vec{a}_j) \cdot \Delta \vec{S} \right]_k \\
&= (l\sqrt{a})^{-1} \left\{ \left[V^1 V^1 \sqrt{a} \vec{a}_1 + V^2 V^1 \sqrt{a} \vec{a}_2 + V^3 V^1 \sqrt{a} \vec{a}_3 \right]_1 \right. \\
&\quad + \left[V^1 V^2 \sqrt{a} \vec{a}_1 + V^2 V^2 \sqrt{a} \vec{a}_2 + V^3 V^2 \sqrt{a} \vec{a}_3 \right]_2 \\
&\quad - \left[V^1 V^1 \sqrt{a} \vec{a}_1 + V^2 V^1 \sqrt{a} \vec{a}_2 + V^3 V^1 \sqrt{a} \vec{a}_3 \right]_3 \\
&\quad - \left[V^1 V^2 \sqrt{a} \vec{a}_1 + V^2 V^2 \sqrt{a} \vec{a}_2 + V^3 V^2 \sqrt{a} \vec{a}_3 \right]_4 \\
&\quad + \frac{l}{d} \left[V^1 V^3 \sqrt{a} \vec{a}_1 + V^2 V^3 \sqrt{a} \vec{a}_2 + V^3 V^3 \sqrt{a} \vec{a}_3 \right]_5 \\
&\quad \left. - \frac{l}{d} \left[V^1 V^3 \sqrt{a} \vec{a}_1 + V^2 V^3 \sqrt{a} \vec{a}_2 + V^3 V^3 \sqrt{a} \vec{a}_3 \right]_6 \right\}
\end{aligned} \tag{29}$$

With the help of equations 11, 12, and 13 \vec{A} can also be expressed for the Cartesian coordinate system as

$$\begin{aligned}
\vec{A} &= \frac{1}{l\sqrt{a}} \vec{i} \left\{ (V^1 V^1 \sqrt{a})_1 + (V^1 V^2 \sqrt{a})_2 - (V^1 V^1 \sqrt{a})_3 - (V^1 V^2 \sqrt{a})_4 + (V^1 W)_5 \right\} \\
&\quad + \frac{1}{l\sqrt{a}} \vec{j} \left\{ (V^2 V^1 \sqrt{a})_1 + (V^2 V^2 \sqrt{a})_2 - (V^2 V^1 \sqrt{a})_3 - (V^2 V^2 \sqrt{a})_4 + (V^2 W)_5 \right\} \\
&\quad + \frac{1}{l\sqrt{a}} \vec{k} \left\{ \left[\sqrt{a} (V^1 V^1 h_x + V^2 V^1 h_y) \right]_1 + \left[\sqrt{a} (V^1 V^2 h_x + V^2 V^2 h_y) \right]_2 \right. \\
&\quad - \left[\sqrt{a} (V^1 V^1 h_x + V^2 V^1 h_y) \right]_3 - \left[\sqrt{a} (V^1 V^2 h_x + V^2 V^2 h_y) \right]_4 \\
&\quad \left. + \left[W (V^1 h_x + V^2 h_y) \right]_5 \right\},
\end{aligned} \tag{30}$$

in which all of the terms of $V^3 V^m$ ($m = 1, 2$, or 3) have been neglected since $V^3 \ll V^1$ or V^2 and equation 28b has been used. V^3 can be large only if h_x and/or h_y in equation 21c is large.

2.3 Empirical Surface Layer Profiles

Accurate calculation of the integrals in equations 8c and 9 for a volume element requires use of surface normal profiles of temperature and wind velocity in the surface layer. The HRW model assumes that the following empirical profiles in the z direction may still be applied locally in the n direction (figure 1). The model has adopted profiles for wind speed and potential temperature as follows:

$$V(z) = V_r \left(\frac{z}{z_r} \right)^m, \quad (31)$$

and

$$\theta(z) = \theta_r + \gamma(z - z_r), \quad (32)$$

where V_r and θ_r denote the wind speed and the potential temperature at a reference height (z_r) which can be the top of the volume element. From these equations note that the potential temperature is assumed linear with height, γ being the gradient, and that the wind speed follows a power law (e.g., Arya, 1999). The value of the exponent m can be estimated from surface layer similarity theory, which defines a non-dimensional wind shear

$$\phi_m(\zeta) = \phi_m \left(\frac{z}{L} \right) = \frac{kz}{u_*} \frac{dV}{dz}. \quad (33)$$

Hence

$$V(z) = \frac{u_*}{k} \left[\ln \frac{z}{z_0} - \int (1 - \phi_m) d \left(\ln \frac{z}{L} \right) \right] = \frac{u_*}{k} \left[\ln \frac{z}{z_0} - \psi_m \left(\frac{z}{L} \right) \right], \quad (34)$$

where z_0 is the roughness length, L is the Obukhov length, and ψ_m is a newly defined function; see Garratt (1992) for details. Panofsky and Dutton (1984) have shown

$$m = \frac{\phi_m \left(\frac{z}{L} \right)}{\ln \frac{z}{z_0} - \psi_m \left(\frac{z}{L} \right)}. \quad (35)$$

The empirical wind shear and wind speed profiles of Businger et al. (1971) have been used by the HRW model. It is impractical, however, to use their original formulation since L and hence the non-dimensional height $\zeta \left(= \frac{z}{L} \right)$ are usually unknown. Instead, an empirical expression for ϕ_m in terms of the Richardson number (Ri) can be used. For example, Ball and Johnson (1978) used the following expression:

$$\begin{aligned} \phi_m &= (1 - 12Ri)^{-\frac{1}{4}}; \quad Ri \leq 0.0 \\ &= (1 - 3Ri)^{-1}; \quad 0.0 < Ri < 0.03571 \\ &= 0.88(1 - 6Ri)^{-1}; \quad 0.03571 \leq Ri \leq 0.1246 \\ &= 1.75(1 - 4Ri)^{-1}; \quad 0.1246 < Ri \leq 0.25 \end{aligned} \quad (36)$$

in which

$$Ri = (Ri)_b + (Ri)_c, \quad (37)$$

where the bulk Richardson number, $(Ri)_b$, is

$$(Ri)_b = \left(\frac{g}{\theta_0} \right) \frac{z(\theta_0 - \theta)}{V_r^2}. \quad (38)$$

$(Ri)_c$ in equation 37 represents the Richardson number for curved flows. This additional Richardson number was originally suggested by Bradshaw (1969) for curvature effects of curved flows,

$$(Ri)_c = 2S(1 + S), \quad S = \left(\frac{V}{R} \right) \left(\frac{dV}{dR} \right). \quad (39)$$

Here R is the radius of streamline curvature. If the average surface normal acceleration A_n in the layer is used and is assumed to be purely centripetal ($-VV/R$), and the average value of $V(dV/dz)$ of equation 31 is used, then S can be approximated by

$$S = -\frac{2A_n z_r}{V_r^2}.$$

2.4 Computational Aspects and Algorithm

The computational aspects of the HRW model are illustrated in figure 2, a simplified computational flow chart. As indicated in figure 2 there are three main stages: (1) data input and model setup; (2) relaxation scheme through direct variation; and (3) model data processing, output and plotting programs. These primary stages are discussed in the following sections.

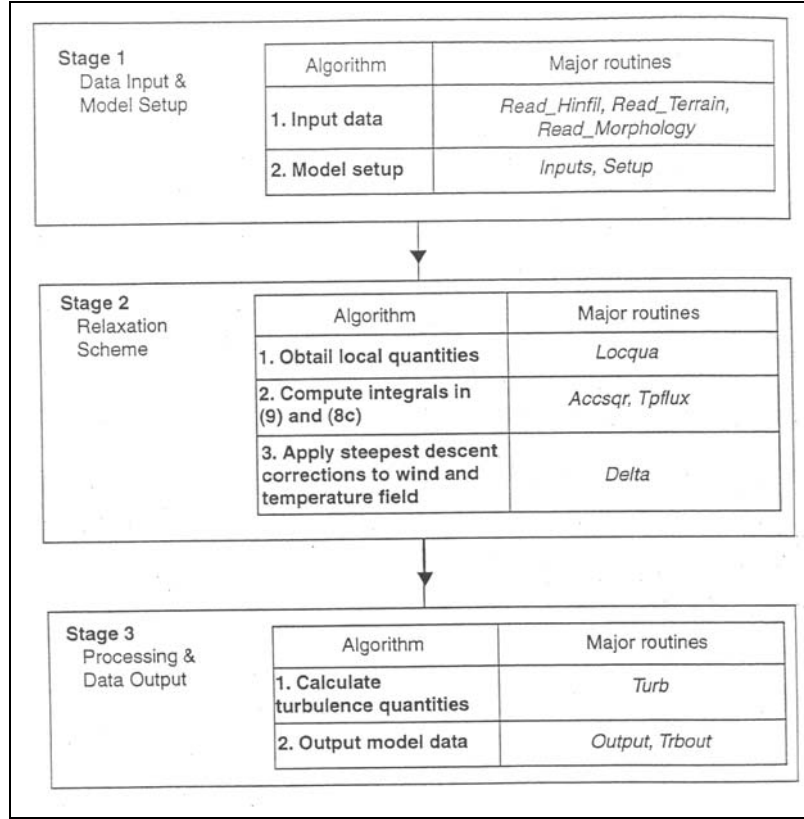


Figure 2. Computational flow chart for the HRW model. This chart illustrates the three essential stages and their major routines.

2.4.1 Data Input and Model Setup

To initiate a model run, necessary input data are required to provide control and driving parameters. Table 1 (upper part) lists the required input data. First, there are a number of control parameters which include the setting of the computation domain, grid system and resolutions, important constants, data handling and storage, etc. Secondly, the computation requires input of digitized terrain data at every grid point, $h(i, j)$ $i, j = 1, 2, 3, \dots, N$. The input file of terrain height for the major routine (Read-Terrain, in figure 2) should be properly formatted. The additional vegetation data, i.e., the vegetation element heights, $h_{veg}(i, j)$, are also needed. In such a case, the effective terrain heights, $h_{eff}(i, j)$, will be calculated as

$$h_{eff}(i, j) = h(i, j) + 0.70 * h_{veg}(i, j).$$

An empirical expression for the roughness length (z_0) over vegetation has been used

$$z_0(i, j) = 0.014 + 0.14 * h_{veg}(i, j),$$

where z_0 is in meters, see Cionco (1983).

Table 1. A list of input and output data for the HRW model.

Input	Category	Notation (unit)	Remark
1	Control parameters And flags	$D(x, y)$, Computation domain $\Delta x, \Delta y$ resolutions grid system, relaxation processes, etc	typically $\Delta x = \Delta y = 100$ m
2	Digitized terrain data	$h(i, j)$, (m)	$i, j = 0, 1, 2, \dots, N$ ($N = 50$)
3	Vegetation data	$h_{veg}(i, j)$, (m)	Vegetation element height
4	Surface station observation	\vec{V}_{sfc} (at 10 m), (ms^{-1}) T_{sfc} (at 10 m), (K) $p(3), T(3), h(3)$ $p(2), T(2), h(2)$ $p(1), T(1), h(1)$	Constant value within D pressure, temperature and geopotential height at three levels, e.g., at 700, 850, mb and at the surface
Output			
1	Calculated wind field	$\vec{V}(i, j)$ (ms^{-1})	defined by (21)
2	Calculated potential temperature field	$\theta_{sfc}(i, j)$ (K)	calculated by (24b)
3	Richardson number	$Ri(i, j)$	defined by (37)
4	Friction velocity	$u_*(i, j)(ms^{-1})$	calculated by (34)
5	Wind profile exponent	m	calculated by (35)

As indicated in table 1, a minimal set of meteorological data is also required to initialize the model. The initial wind field (\vec{V}_{sfc}) is obtained either by local meteorological observation of wind speed and direction (at 10 m height) or by an estimation of the geostrophic wind near the surface. The model assumes a homogeneous initial wind field, i.e., the initial velocity \vec{V}_{sfc} , is constant throughout the computational domain. On the other hand, the initial potential temperature, $\theta_{sfc}(i, j)$, varies within the domain. To calculate the initial field of $\theta(i, j)$, the following algorithm has been adopted.

(a) Using the upper air sounding as the input data, the ambient potential temperature (θ_0) as defined by equation 5 is derived by extrapolating the background potential temperature profile to the surface. For example

$$\theta_0 = \theta_{850} + (h_{sfc} - h_{850}) \frac{(\theta_{850} - \theta_{700})}{h_{850} - h_{700}}, \quad (40)$$

where θ_{850} and θ_{700} are the potential temperature at the 850 and 700 mb, respectively. Further, h_{sfc} , h_{850} , and h_{700} refer to the geopotential height at the surface, 850 and 700 mb, respectively, and h_{sfc} is also the altitude of the sounding station.

(b) Also using the upper air sounding and the terrain height data, $h(i, j)$, the surface pressure at each grid point is calculated by a linear extrapolation, e.g.,

$$p(i, j) = 850 + [h(i, j) - h_{850}] \frac{(850 - 700)}{h_{850} - h_{700}},$$

where the $p(i, j)$ has the unit of *mb*.

(c) To calculate the surface heating (ΔQ) as an input parameter from equation 24

$$\Delta Q = \frac{dq}{c_p} = T_{sfc} \frac{(\theta_{sfc} - \theta_0)}{\theta_0}, \quad (24a)$$

where the surface temperature (T_{sfc}) and the surface potential temperature (θ_{sfc}) are obtained from observation of a surface meteorological station.

(d) It is assumed that the value of ΔQ from a single (station) observation is representative for the whole domain. This assumption means the right hand side of equation 24a can be applied to any grid point (i, j) . Thus

$$\theta_{sfc}(i, j) = \theta_0(i, j) + \Delta Q \left[\frac{\theta_0(i, j)}{T_{sfc}(i, j)} \right] \approx \theta_0(i, j) + \Delta Q \left[\frac{1000}{p(i, j)} \right]^{0.286}, \quad (24b)$$

where the ambient background potential temperature at a gridpoint (i, j) can be extrapolated from the sounding data, equation 40.

$$\theta_0(i, j) = \theta_{850} + [h(i, j) - h_{850}] \frac{\theta_{850} - \theta_{700}}{h_{850} - h_{700}}. \quad (24c)$$

Lanicci (1985) has discussed the calculation of the ΔQ and has suggested some modifications. For a location where $h_{sfc} > h_{850}$, we will use the sounding data at higher levels, e.g., 500 and 700 mb instead of at lower levels, e.g., 700 and 850 mb.

2.4.2 Relaxation Scheme

As indicated by figure 2, the central stage of the HRW model computation is the relaxation scheme, which is the workhorse of the model. The scheme implements the calculation of the integrals, equations 8c and 9 as well as the variational technique to find the minimum of equation 9. As mentioned in section 2.2, the evaluation of the integral in equation 9 adopts computational elements called flux boxes. Consequently, the total constraint integral of equation 9 can be expressed as a sum over all flux boxes in the modeled area

$$R_T = \sum_{i,j} R_{ij} = \sum_{i,j} \left(\vec{A} + b \vec{g}_s \right)_{i,j}^2. \quad (9a)$$

For variational purposes we consider the $R_{i,j}$, called residues, as functions of only the two velocity components $(V^1, V^2)_{i,j}$ at the grid point (i, j) . Denoting the two velocity components at each grid point by $V_{i,j}^k (k = 1, 2)$, the unit vector of global steepest descent in this two-dimensional velocity space is written as

$$n_{i,j}^k = - \frac{\frac{\partial R_{i,j}}{\partial V_{i,j}^k}}{\left[\sum_{i,j} \left[\sum_k \left(\frac{\partial R_{i,j}}{\partial V_{i,j}^k} \right)^2 \right] \right]^{\frac{1}{2}}}. \quad (41)$$

The steepest descent method computes a velocity correction $(\Delta V_{i,j}^k)$ proportional to the steepest descent unit vector for each relaxation sweep over the entire grid. This velocity correction has been chosen as

$$\Delta V_{i,j}^k = C_r \cdot V_r \sqrt{N \cdot M} n_{i,j}^k$$

where C_r is a selected fraction of a velocity scale, V_r . Currently $C_r = 0.02$ and V_r is the constant initial wind speed or 2 ms^{-1} , whichever is greater. N and M are the grid dimensions, currently $N = M = 51$. All velocity corrections are applied simultaneously at the end of each sweep. This implies the velocity field after each relaxation step is

$$V_{i,j}^1 = V_{i,j}^1 + \Delta V_{i,j}^1, \quad V_{i,j}^2 = V_{i,j}^2 + \Delta V_{i,j}^2.$$

This relaxation algorithm apportions larger corrections to regions of the grid where the constraint integral is most sensitive to changes in the velocity field. The relaxation scheme calculates the total constraint R_T at each relaxation sweep and saves the wind field for the minimum value of R_T achieved. Each relaxation sweep also adjusts the potential temperature field by use of equation 8c. Consequently each relaxation sweep yields altered potential temperature and velocity fields until equation 9 is satisfied.

2.4.3 Data Output

The final stage of the model computation produces various computational results. As shown in table 1, the output data comprises at least five categories. The most important output is, of course, the surface layer wind field. It should be stressed that the calculated windfield refers to the three components in the terrain following warped coordinate system since the model is formulated according to such a unique coordinate system. It is, however, easy to transform these three components (V^1, V^2, V^3) into Cartesian wind components (u, v, w) as indicated by equation 21. The second category of output is the calculated field of surface potential temperature which can also be transformed into surface temperature easily. Finally the other three categories of output are related to turbulence characteristics (u_* and Ri) and the exponent

(*m*) of the power law of wind profiles in the surface layer. During the past decade several versions of algorithms and programs for output displays and plotting have been tested and established. Those aspects related to the software developments will not be discussed in this report.

3. Results of the Model Evaluation

3.1 The MADONA Data

The micrometeorological data used in this evaluation study are based on measurements during the field study of MADONA in September 1992. Cionco et al. (1999) have provided a comprehensive overview of the MADONA project including its database. The MADONA field site is located at Porton Down, near Salisbury, United Kingdom. From 14 to 23 September 1992, there were ten days of intensive measurements. Extensive high-resolution micrometeorological data were collected to complement the diffusion data. Fifteen sets of standard wind speed (three cup anemometer) and wind direction (vane anemometer) sensors were deployed at 14 locations by the UK Chemical and Biological Defence Establishment (CBDE, now part of the Defence Evaluation and Research Agency). These wind sensors were calibrated before and after the field measurements. Figure 3 illustrates the locations of these wind measurement stations (M1 through M15) plotted on terrain contours. All wind sensors except M9 were mounted at 10 m above the ground. The M9 station was installed at 30 m above the ground at the same tower as M8 to provide dual measurements at the same location. The area covered by figure 3 is 5 by 5 km, which is the domain for the HRW simulations. The wind data from M1 and M3 are excluded for model evaluation because their locations are very close to the model boundary, and the data from M8/9 are not used due to technical reasons. Altogether the measured wind data from eleven locations (Station M2, M4–7, and M10–15) are used for the comparison between the measurements and the HRW simulations. All the wind data, as well as other MADONA data including the area terrain data, have been officially documented on CD-ROM. The CD-ROM includes the averages of wind speed and direction for 5 min, 10 min, 30 min, and 60 min, among other statistics. The 5 min averages of wind measurements at 10 m above the ground from these 11 locations are those used for the present study. Unfortunately, there were no corresponding temperature sensors at the same 11 stations provided by CBDE due to financial constraints. The CD-ROM is available on request from the RISO National Laboratory, P.O. Box 49, Roskilde, Denmark.

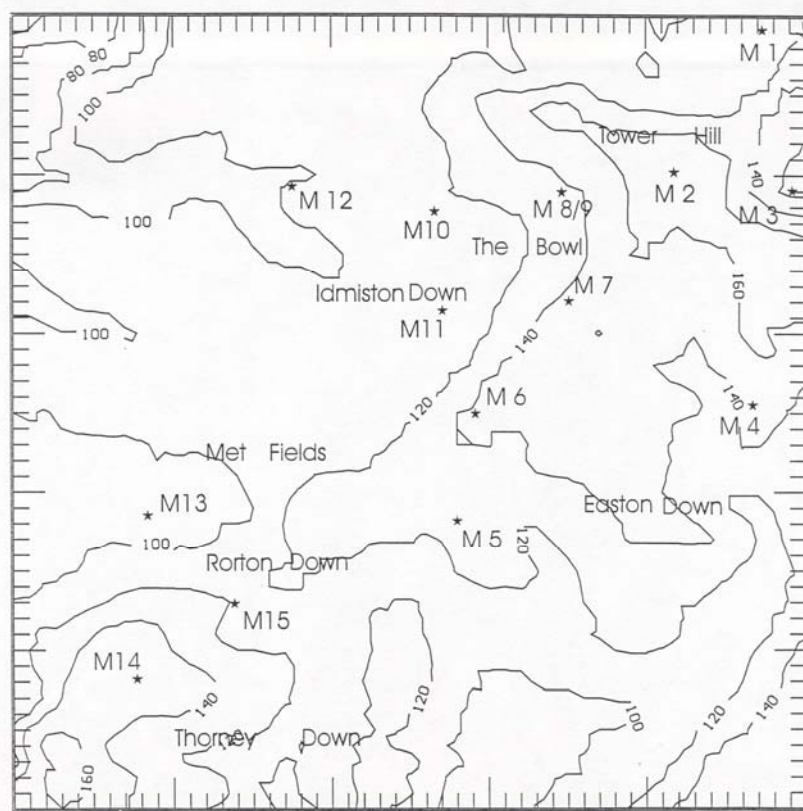


Figure 3. Locations of MADONA measurements sites (M1 through M15) plotted on terrain contours.

As shown in figure 3, the topography at the MADONA site is gently rolling terrain with a ridge running southwest to northeast (approximately 230° – 50°) with higher terrain at each end. Total relief for the domain is about 100 m from 80 m northwest to 180 m near Tower Hill. In such a small area, however, the wind distribution inhomogeneity is significant, as shown by Cionco et al. (1999, their figures 7 and 8). Generally, the wind speeds over the ridge (e.g., M14) are stronger, while over the lower land (e.g., M13) they are weaker.

3.2 The Model Simulations

During the ten days of intensive measurements from 14 to 23 September 1992, a series of boundary layer soundings were launched for each date from the middle of the MADONA experimental area, as described by Cionco et al. (1999). Also, traditional upper air soundings from the UK Meteorological Office Larkhill station and surface meteorological observations from CBDE's Met office were available during the experiment. These sounding and surface observation data (surface temperature at 10 m AGL in particular) provide the necessary inputs for the HRW simulations. The wind data measured at Station M10 are used to initialize the wind field for model runs. Table 2 lists the 39 model runs chronologically during these 10 days. The surface heating (ΔQ) in table 2 is calculated from equation 24a. The wind speed and direction in table 2 are the initialized values which are the 5 min averages of the observed wind at Station M10, located in the middle of the diffusion study area.

Table 2. The 39 cases for the HRW simulations. ΔQ is defined by equation 24a in the text.

CaseNo.	Day (1992)	Local Time	ΔQ (K)	Wind Speed (ms^{-1})	WindDirection (degree)
1	14 Sept	14:10'	9.21	5.4	261
2		15:55'	9.78	7.2	280
3		17:20'	2.58	4.0	270
4	15 Sept	12:10'	-5.10	8.0	240
5		13:55'	-2.50	7.5	240
6		15:55'	-2.70	7.4	245
7		17:40'	2.98	5.5	240
8	16 Sept	10:30'	-2.45	3.0	120
9		13:55'	-3.45	0.3	90
10		16:10'	-5.45	3.0	160
11		17:50'	-5.52	2.0	160
12	17 Sept	10:30'	-6.54	5.0	130
13		14:15'	-5.65	1.0	180
14		17:25'	-4.02	5.5	180
15	18 Sept.	10:30'	-0.54	4.5	280
16		13:10'	-0.88	4.0	255
17		14:55'	-2.34	3.0	250
18		18:15'	0.00	2.5	170
19	19 Sept	10:30'	3.88	4.0	260
20		12:10'	6.12	5.0	270
21		14:00'	6.59	5.0	270
22		16:10'	5.94	4.5	275
23		18:25'	3.56	1.5	250
24	20 Sept	10:30'	3.73	4.5	220
25		12:40'	10.26	2.5	225
26		14:45'	5.39	2.5	225
27		15:55'	3.86	2.0	200
28	21 Sept	10:30'	-0.20	7.5	70
29		14:25'	1.29	4.5	110
30		15:25'	-1.35	3.5	140
31		18:00'	-1.83	3.5	160
32	22 Sept	10:30'	1.11	0.5	320
33		13:30'	7.32	1.2	295
34		15:10'	2.20	2.5	360
35	23 Sept	10:30'	5.44	6.0	280
36		12:00'	8.78	7.5	275
37		14:15'	8.76	8.5	270
38		16:10'	9.71	5.0	280
39		17:40'	1.48	2.5	250

As mentioned before, the domain of the model simulation is 5 by 5 km with a spatial resolution of 100 m. Thus, there are 2601 (51 times 51) grid points covered by the computation domain. Only the simulated wind speeds and directions at the 11 gridpoints corresponding to the 11 measurement locations have been chosen for comparison. To evaluate the model performance, the simple linear regression analysis is used as follows

$$y = ax + b \quad (42)$$

where x is the observed value of either wind speed or wind direction, and y is the corresponding simulated value from the model runs. The terms a and b represent the slope and intercept of the regression line, equation 42, respectively. For each run (case) listed in table 2, there are generally 11 pairs (datapoints) of (x, y) . However, there are only 10 datapoints for case 9, and 9 datapoints for case 23. In these two cases, the observed wind speeds from M12 (case 9) and from both M12 and M13 (case 23) were zero. Consequently, the wind direction is undetermined for these two cases. Therefore, the total number of (x, y) datapoints from the 39 cases is 426 for the simultaneous wind direction and speed evaluation. For a single station, except M12 and M13, on the other hand, there are 39 datapoints for the linear regression analysis. A correlation coefficient (r) and a standard deviation (S) for a set of (x, y) datapoints can also be calculated. The linear regression should yield $a = 1$, $b = 0$, $r = 1$, and $S = 0$ for an ideal or perfect model. In reality, however, no model is perfect. The values of a , b , r , and S can help evaluate the model performance under various circumstances.

3.3 The Results of Linear Regression Analysis

(1) Figures 4a and 4b present the simulated winds from the 39 cases versus the observed winds in scatter diagrams with the regression line equation 42 superimposed. Figure 4a is for the wind direction comparison, while figure 4b is for the wind speed comparison. Both figures show the plot for all 11 stations together as well as for individual stations. Table 3 lists the values of a , b , r , and S corresponding to figures 4a and 4b. From the total 426 datapoints, the values of a , b , r , and S are 1.004, 2.000, 0.970, and 16.3° , respectively for the wind direction, and 0.868, 0.902, 0.857, and 1.02 ms^{-1} , respectively for the wind speed, as shown in table 3. This result has been partially reported by Cionco and Byers (1995). Therefore, the HRW model simulations as a whole appear to provide quite high positive correlations, especially for the wind direction. For individual stations, r is always greater than 0.96 for wind direction and greater than 0.80 for wind speed, as indicated in table 3. The model performs fairly well for each of the 11 locations, although it appears to perform better for certain locations (e.g., M10, M11) than for other locations (e.g., M15, M14), as seen from figure 4 and table 3. The model does not demonstrate significant failure at any particular location. It is also evident that the model simulations appear better for wind direction than for wind speed. As for an individual case, the model sometimes simulates a case satisfactorily, but not always. A statistical result for each individual case is meaningless due to small number of data points, and hence is not presented.

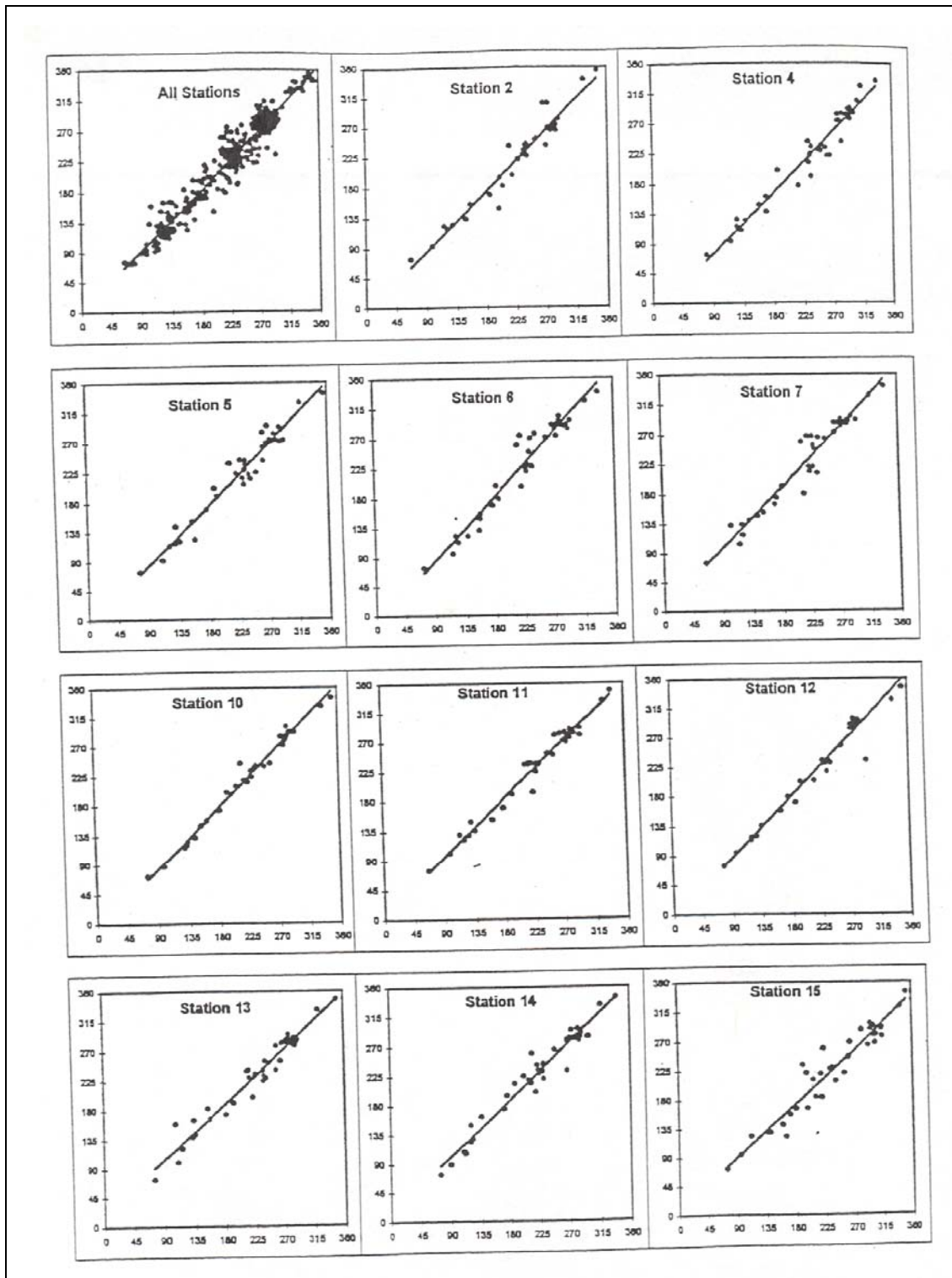


Figure 4a. Scatter diagrams for simulated wind direction (y, degree) versus observed values (x, degree). The straight lines result from the linear regression analysis, equation 42.

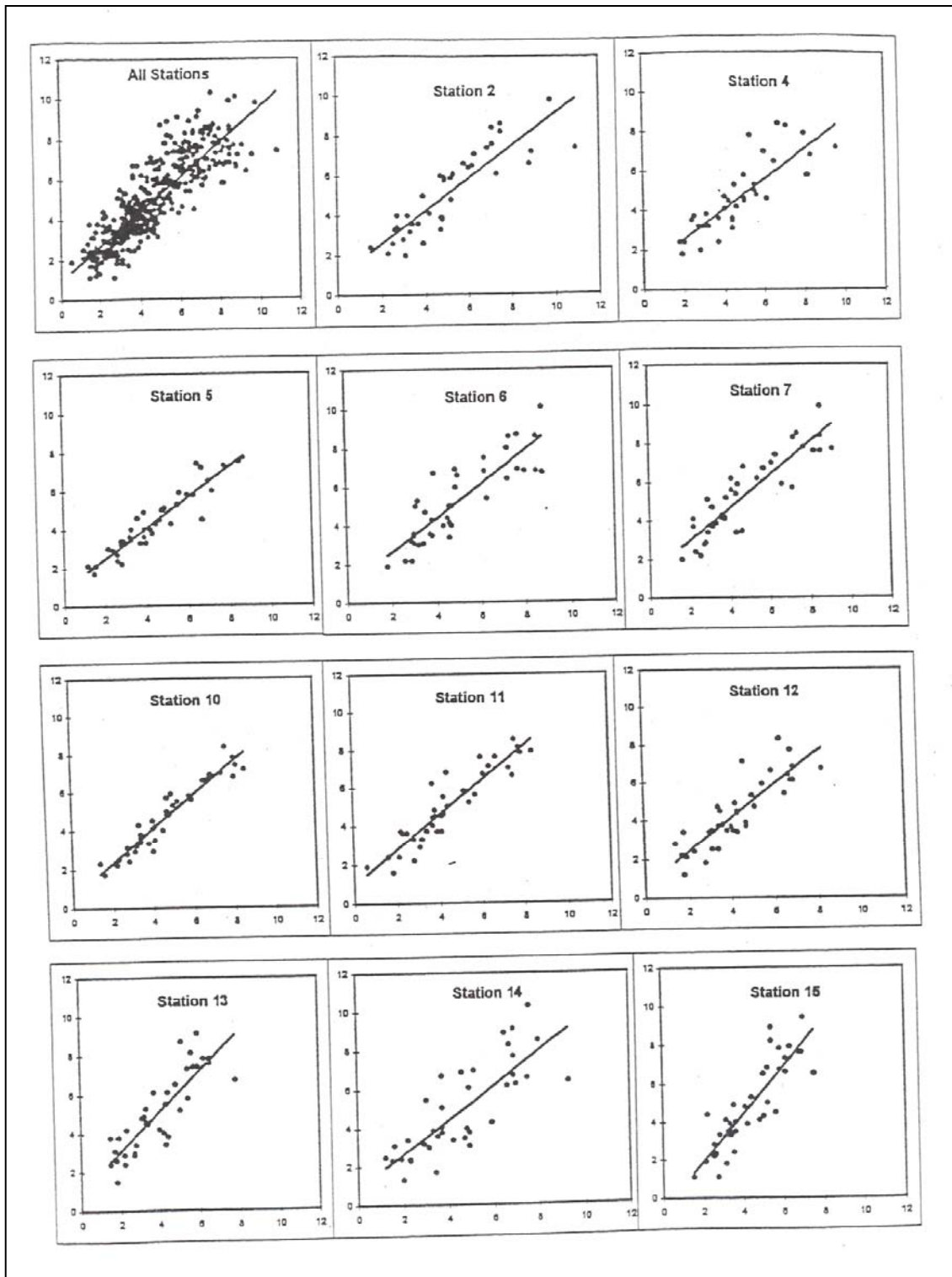


Figure 4b. Scatter diagrams for simulated wind speed (y , ms^{-1}) versus observed values (x , ms^{-1}). The straight lines result from the linear regression analysis, equation 42.

Table 3. The value of n (data pair number), a (slope), b (intercept), r (correlation coefficient), and S (standard deviation) from the linear regression equation 42, for wind direction and wind speed, respectively.

Station	n	Wind direction (degree)				Wind speed (ms^{-1})			
		a	b	r	S	a	b	r	S
M2	39	1.0116	-5.3141	0.9716	15.9	0.8169	0.9626	0.8739	1.02
M4	39	1.0288	-7.0611	0.9762	15.1	0.7601	1.0301	0.8358	1.00
M5	39	1.0241	-8.4746	0.9759	14.7	0.7964	0.8659	0.9397	0.57
M6	39	1.0795	-11.2393	0.9676	17.9	0.8728	0.8877	0.8582	1.07
M7	39	1.0278	5.9955	0.9697	17.0	0.8448	1.2949	0.8942	0.92
M10	39	1.0386	-10.035	0.9926	8.3	0.8951	0.5111	0.9586	0.52
M11	39	0.9833	7.5243	0.9862	11.0	0.3993	0.9655	0.9255	0.73
M12	37	1.0344	-5.6589	0.9778	14.8	0.8725	0.6401	0.8629	0.90
M13	38	0.9391	20.405	0.9742	14.9	1.0292	1.0245	0.8502	1.07
M14	39	0.9631	15.7441	0.9775	14.5	0.8834	0.8918	0.8038	1.40
M15	39	0.9255	7.0691	0.9613	18.7	1.2376	-0.5478	0.8708	1.11
All	426	1.0043	2.0001	0.9701	16.3	0.8681	0.9024	0.8567	1.02

(2) To further investigate the model performance, comparisons of wind field between simulations and observations for different wind directions and different wind speeds have been conducted. The 39 cases listed in table 2 have been grouped into three categories of wind direction and three categories of wind speed. The criteria for wind direction categorization take into account the general ridge direction in the MADONA area, which is approximately 230° – 50° , as mentioned earlier (see figure 3). The three wind direction (WD) categories are defined as

1) Parallel to the ridge (14 cases),

$$200^\circ < WD < 260^\circ \quad \text{or} \quad 20^\circ < WD < 80^\circ \quad (43a)$$

2) Perpendicular to the ridge (10 cases)

$$110^\circ < WD < 170^\circ \quad \text{or} \quad 290^\circ < WD < 350^\circ \quad (43b)$$

3) Slant to the ridge (15 cases)

$$350^\circ < WD < 20^\circ \quad \text{or} \quad 80^\circ < WD < 110^\circ \\ \text{or} \quad 170^\circ < WD < 200^\circ \quad \text{or} \quad 260^\circ < WD < 290^\circ \quad (43c)$$

The three wind speed (WS) categories are defined more or less subjectively. They are

1) Light wind (15 cases),

$$WS \leq 3.0 \text{ ms}^{-1} \quad (43d)$$

2) Moderate wind (16 cases),

$$3.0 \text{ ms}^{-1} < WS < 6.0 \text{ ms}^{-1} \quad (43e)$$

3) Strong wind (8 cases),

$$WS \geq 6.0 \text{ ms}^{-1} \quad (43f)$$

The results of these comparisons are presented in table 4. They are also shown in figure 5 for the three wind direction categories, and in figure 6 for the three wind speed categories, respectively.

Table 4. Same as table 3 except for three wind direction categories as defined by equation 43 (a, b, c) and three wind speed categories as defined by equation 43 (d, e, f).

Category	<i>n</i>	Wind Direction (degrees)				Wind Speed (ms ⁻¹)			
		<i>a</i>	<i>b</i>	<i>r</i>	<i>S</i>	<i>a</i>	<i>b</i>	<i>r</i>	<i>S</i>
Wind direction:									
Parallel	152	0.9684	11.7935	0.9335	17.8	0.7946	0.9584	0.8878	0.90
Perpendicular	110	1.0028	-1.5884	0.9737	15.4	0.7447	1.1904	0.7117	0.83
Slant	164	0.9530	16.7129	0.9484	14.9	0.9111	1.0255	0.8144	1.12
Wind speed:									
Light	162	0.9787	6.5416	0.9452	21.8	0.7949	0.9477	0.6617	0.79
Moderate	176	1.0271	-1.5462	0.9829	12.4	0.8645	1.0031	0.7293	1.04
Strong	88	1.0013	1.1356	0.9888	10.0	0.1479	6.3077	0.1507	1.04

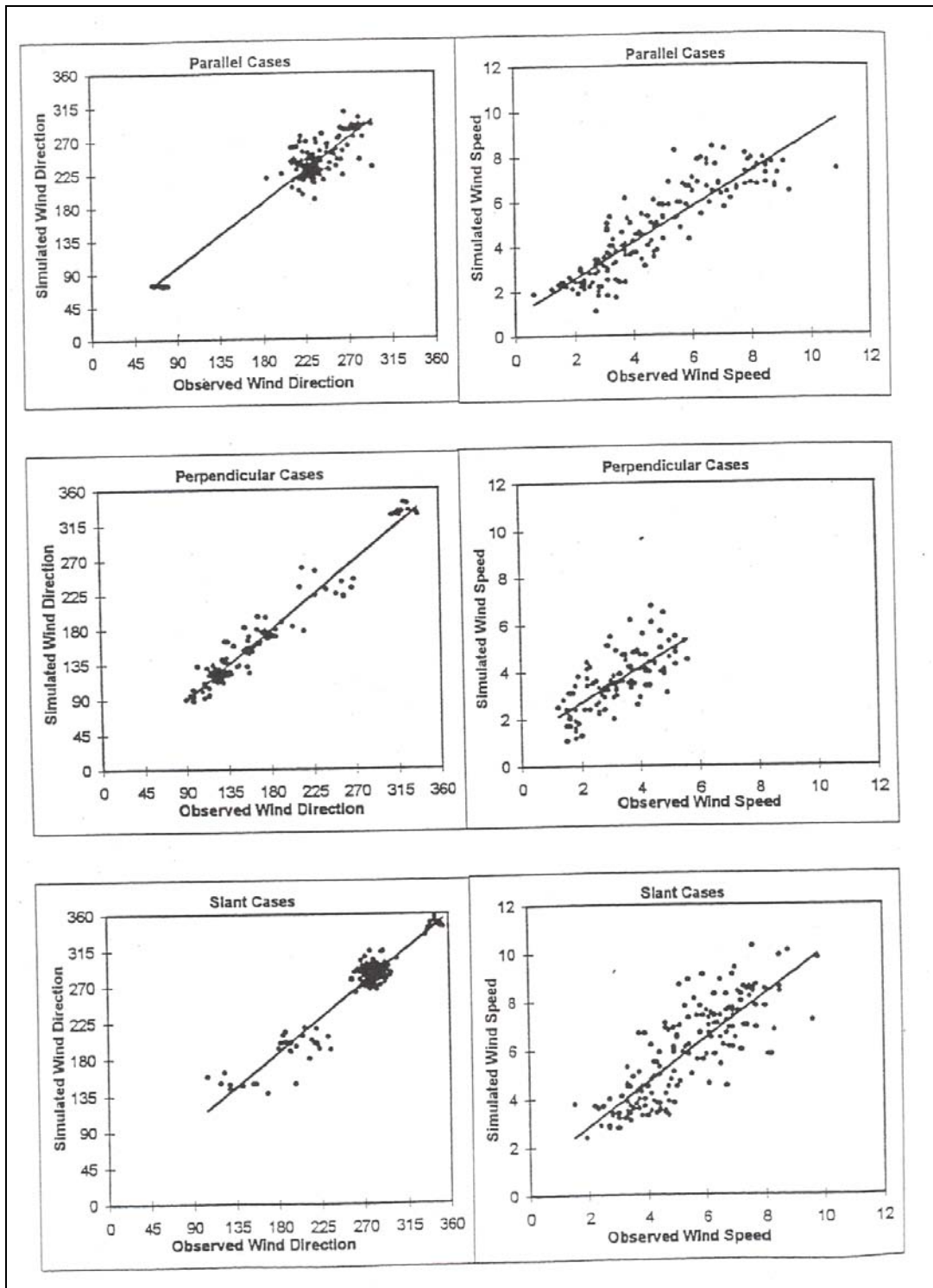


Figure 5. Same as figure 4a except for three wind direction categories as defined by equation 43a, b, c.

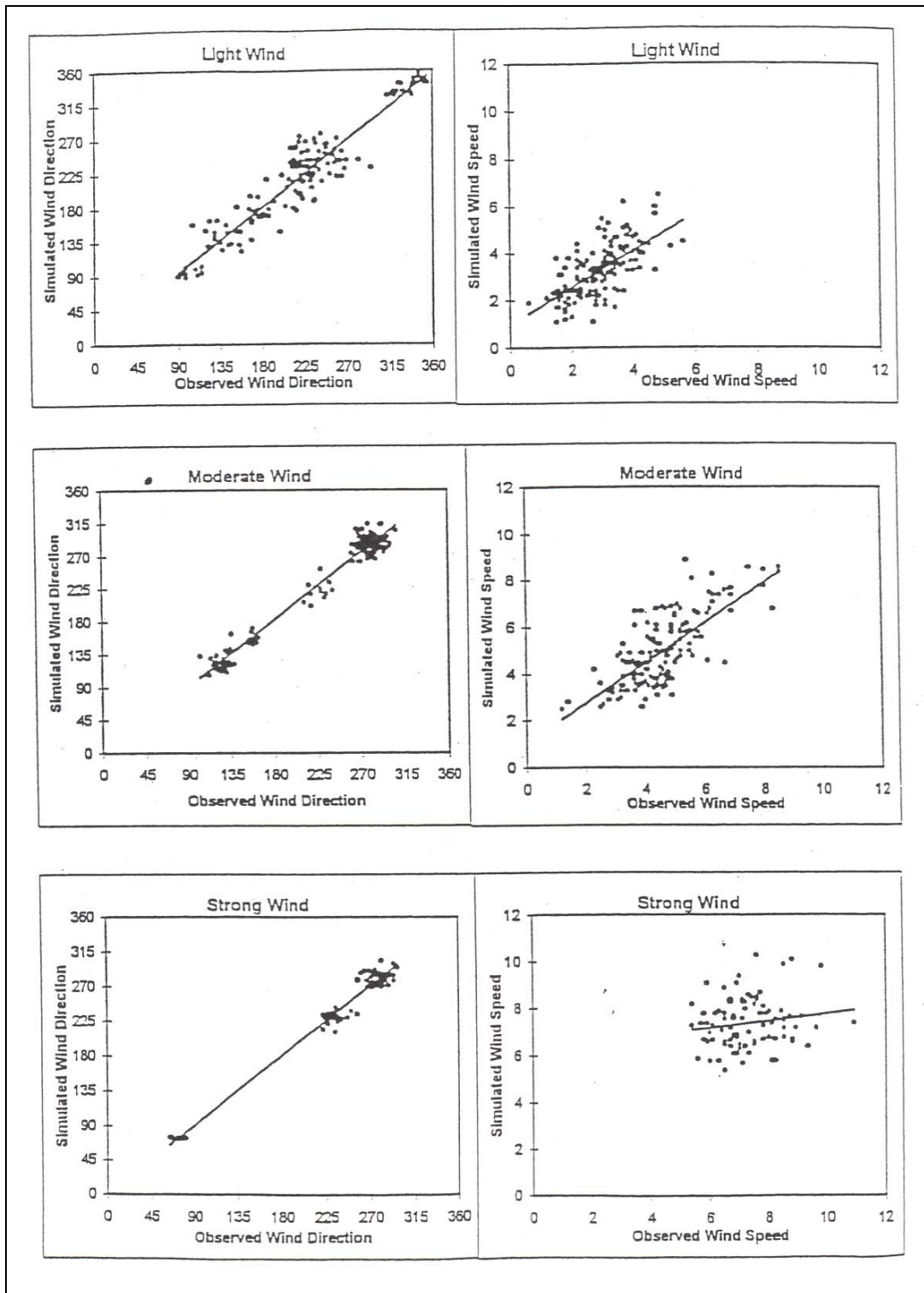


Figure 6. Same as figure 4b except for three-wind speed categories as defined, by equation 43d, e, f.

It appears from table 4 and figure 5 that the model performed better for the perpendicular wind direction category with the highest value of r (0.974) for wind direction and the lowest value of S (0.83 ms^{-1}) for wind speed. It is conceivable that the airflow will experience more acceleration or deceleration when its direction is perpendicular to a ridge. Consequently, the magnitude related to the \overline{A} term in equation 9 will be more significant as compared to the parallel or slant wind directions. For the three categories based on wind speed, figure 6 and table 4 reveal an unsatisfactory situation for the strong wind category. The scatter diagram at the right lower corner of figure 6 shows that the datapoints are scattered around the regression line with low value of r (0.1507) and high value of S (1.04 ms^{-1}) although the simulations for the wind direction appear much better than for the wind speed. This result receives more discussion in the following subsection.

(3) Finally, the 39 cases have also been grouped in terms of atmospheric stability for model performance evaluation. Based on the value of ΔQ , equation 24a, the following three stability categories are defined as

1) Unstable (19 cases),

$$\Delta Q > 2.0^\circ \quad (44a)$$

2) Near-neutral (9 cases),

$$|\Delta Q| \leq 2.0^\circ \quad (44b)$$

3) Stable (11 cases),

$$\Delta Q < -2.0^\circ \quad (44c)$$

The results for the three stability categories are shown in figure 7 and table 5. Among the three atmospheric stability categories, the model appears to perform the best for the near-neutral stratification as compared to unstable or stable stratification. For example, both values of r for wind direction and speed are the highest for the near-neutral category. This result will be discussed in the next section.

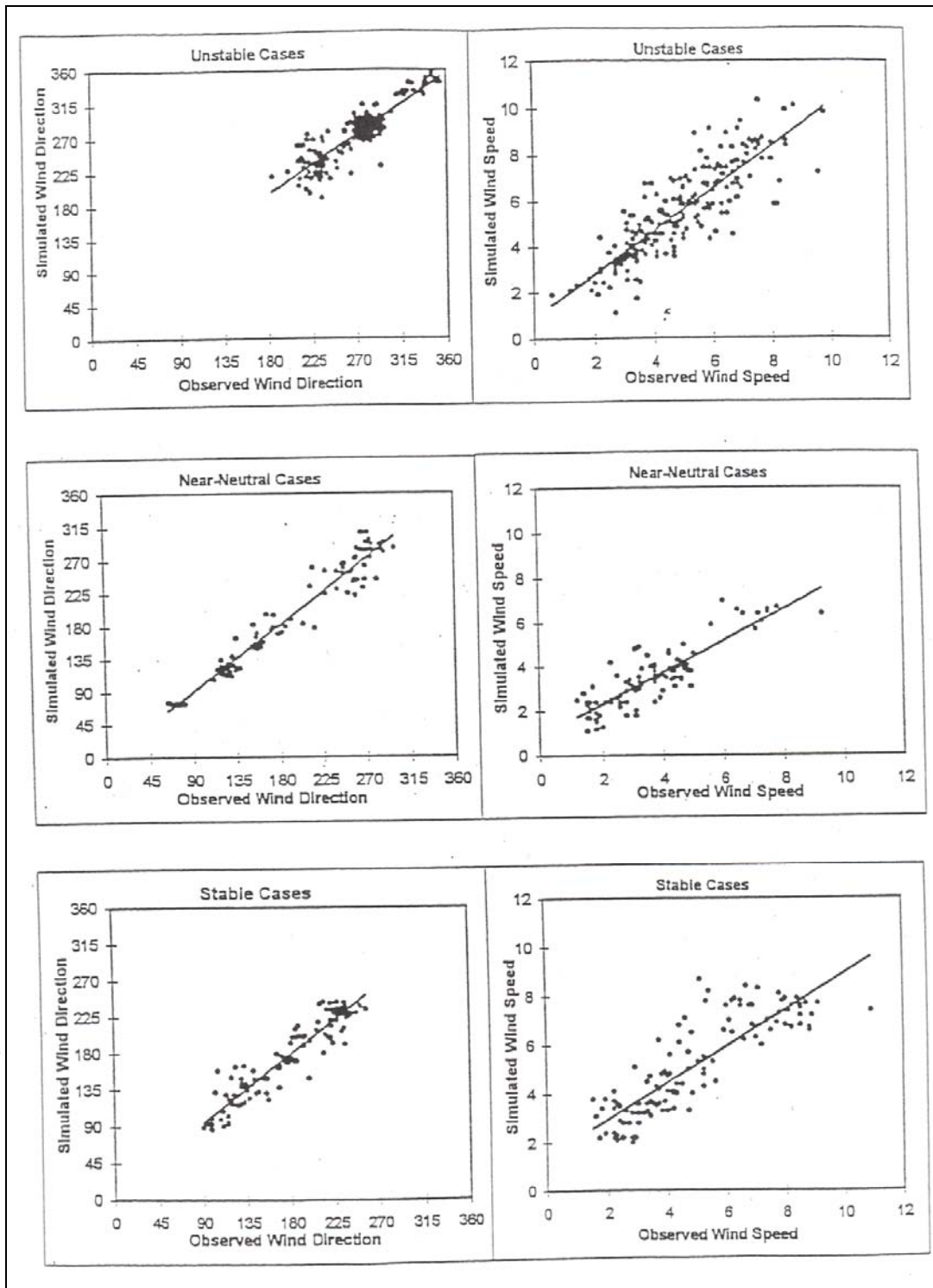


Figure 7. Same as figure 4 except for three stability categories as defined by equation 44a, b, c.

Table 5. Same as table 3 except for three atmospheric stability categories defined by equation 44a, b, c.

Category	n	Wind direction (degree)				Wind speed (ms^{-1})			
		a	b	r	S	a	b	r	S
Unstable	207	0.8949	33.8784	0.8881	15.7	0.9291	0.9063	0.8561	1.00
Near-neutral	99	1.0112	-0.4089	0.9759	16.4	0.7165	0.8671	0.8711	0.67
Stable	120	0.9379	11.1184	0.9444	16.0	0.7445	1.4706	0.8512	1.01

3.4 Discussion

(1) As presented in the last subsection, the HRW model simulates the wind field better for the near-neutral condition than for either stable or unstable conditions. This is because under neutral conditions ($b = 0$) the buoyancy acceleration plays no role and the wind field is influenced by topography only. This result implies that the buoyancy (b) term is important and that a realistic representation of this term for the model is a challenge. As defined by equations 24 and 24a, the calculation of the buoyancy factor (b) or the surface heating (ΔQ) involves the background (reference) potential temperature (θ_o), the surface air temperature (T_{sfc}), and the related surface air potential temperature (θ_{sfc}). The calculation of these three input parameters is not trivial. Currently θ_o is calculated through a linear extrapolation from the potential temperature at 700 mb and 850 mb obtained from a nearby radiosonde observation. In addition, the current algorithm uses ΔQ as input parameter for calculation of T_{sfc} or θ_{sfc} , which can be quite variable over complex terrain. The HRW model employs a low level of sophistication and does not invoke a surface energy balance scheme to deal with surface temperature. It has also been noted that the model is essentially a single surface layer model which decouples this layer from the rest of the boundary layer. This simplification imposes inherent difficulty for the representation of θ_o . Lanicci (1985) had suggested a modified technique for calculation of θ_o , T_{sfc} , and θ_{sfc} . His technique, however, was not verified by observations. Preliminary tests of model sensitivity to atmospheric stabilities (changes in ΔQ or b) have been conducted by one of the authors (Huynh). Those tests show that the HRW simulation is more sensitive to the change in surface heating or surface temperature under stable conditions than it is under unstable conditions. Results of those sensitivity studies will be reported elsewhere.

(2) The results presented in the previous subsection indicate that the HRW model simulates the wind direction field with less error than the wind speed field for the MADONA. A brief discussion of the relative error of the wind direction (E_D) and of the wind speed (E_S) appears useful. These relative errors and its ratio (R_{DS}) are defined as

$$E_D = \frac{dD}{D}, \quad E_S = \frac{dS}{S}, \quad R_{DS} = \frac{E_D}{E_S}, \quad (45)$$

where dD and dS denote the errors of wind direction (D) and wind speed (S), respectively, and

$$S^2 = u^2 + v^2, \quad D = \text{const.} - \phi, \quad \phi = \arctan(v/u), \quad (46)$$

where u and v are defined as eastward and northward component of the wind vector, respectively according to meteorological convention. Similarly, the relative errors in u and v , and their ratio (R_{uv}) are defined as

$$E_u = \frac{du}{u}, \quad E_v = \frac{dv}{v}, \quad R_{uv} = \frac{E_u}{E_v}. \quad (47)$$

A relationship between R_{DS} and R_{uv} can be derived. Equations 48 and 49 can be derived from the definitions of equations 45, 46, and 47

$$E_S = \frac{u^2}{S^2} \left(\frac{du}{u} \right) + \frac{v^2}{S^2} \left(\frac{dv}{v} \right) = \frac{u^2}{S^2} E_u + \frac{v^2}{S^2} E_v. \quad (48)$$

$$E_D = -\frac{1}{D} d \left[\arctan \left(\frac{v}{u} \right) \right] = \frac{uv}{DS^2} (E_u - E_v). \quad (49)$$

Equation 50 may be derived from the two equations above

$$R_{DS} = \frac{1}{D} \frac{(E_u - E_v)uv}{u^2 E_u + v^2 E_v} = \frac{1}{D} \frac{(R_{uv} - 1) \tan \phi}{(R_{uv} + \tan^2 \phi)}. \quad (50)$$

The wind direction (D) in equation 50 is defined in the range: $0 < D < 2\pi$. For the MADONA simulations, $D > \pi/3 = 1.0472$, see figure 4. Therefore, the following relation is true

$$|R_{DS}| < \left| \frac{(R_{uv} - 1) \tan \phi}{R_{uv} + \tan^2 \phi} \right|. \quad (51)$$

Note that $R_{uv} \geq 0$ if du and dv result only from wind speed errors. A positive error in wind speed ($dS > 0$) causes positive E_u and E_v while a negative error ($dS < 0$) results in negative E_u and E_v . Consequently, the absolute value of R_{DS} can be estimated from equation 51.

$$|R_{DS}| < \begin{cases} |1 - R_{uv}| & \text{for } |\tan \phi| > 1 \\ |1 - R_{uv}^{-1}| & \text{for } |\tan \phi| < 1 \end{cases} \quad (52)$$

The above expression implies that $|R_{DS}|$ is < 1.0 when $0.5 < R_{uv} < 2.0$. Only if R_{uv} is either large or small, out of the above range, can the relative errors in wind direction estimation be greater than the relative errors in wind speed estimation. This situation is likely to occur when the wind direction is east, west ($v = 0$), south, or north ($u = 0$). For the MADONA simulations, such wind directions occur infrequently. Consequently, the statistical results for wind direction simulations appear better than for wind speed simulations. The above argument, however, is not intended to

provide a physical explanation for our results. Cauchey et al. (1979), for example, have formulated a wind direction budget equation. A similar wind speed budget equation is not difficult to derive. It is, however, beyond the scope of the present study to analyze these physical budgets.

(3) Finally, the performance of the model simulations for the strong wind speed category seems undesirable. There are eight cases in this category, equation 43c. They are cases 2, 4, 5, 6, 28, 35, 36, and 37 (table 2). As shown in figure 6 (the lowest right panel), the datapoints are scattered around the regression line. The correlation coefficient (r) for the wind speed is 0.1507 (table 4). The difference between the simulated and observed wind can be as large as 27 degrees in wind direction and 3.5 ms^{-1} in wind speed, the extremes at an individual station.

A careful examination of each of these eight cases indicates that the wind fields at the time of the simulations all exhibit significant unsteadiness. There were considerable variations (accelerations) of wind vector, especially wind speed, around the time of the simulations, i.e., considerable $\partial \vec{V} / \partial t$. If there is a gusty wind under a strong wind speed situation, a 1 ms^{-1} of wind speed change in a period of 5 min, then this fluctuation alone is equivalent to an acceleration on the order of 10^{-3} ms^{-2} , which can be greater than the magnitude of acceleration induced by topography or buoyancy. Recall that the HRW model is not a prognostic model, just a diagnostic one, which is applied to a steady wind field. It comes with no surprise then that the model will perform less satisfactorily for gusty (unsteady) wind fields.

4. Conclusions

We have presented a comprehensive description of the high resolution wind model which has been an undertaking at the U.S. Army Research Laboratory (formerly U.S. Army Atmospheric Sciences Laboratory) for three decades. From the early effort of model development, several requirements have been kept in mind: (1) the model can be applied over very complex terrain with limited meteorological information (inputs); (2) the model is adaptable to small horizontal grid spacing on the order of 100 m for a horizontal domain smaller than 10 by 10 km; (3) the model is to be run as a combined system with existing atmospheric dispersion and transport models; (4) the model can be used on a small computer. Our HRW model uses Gauss's Principle of least constraint for a variational adjustment of an initial estimated wind field in a single surface layer to conform with terrain structures, mass conservation, and buoyancy forces. This basic approach and its features appear to meet the above requirements.

The measurements from the field study of Meteorology and Diffusion Over Non-Uniform Areas (MADONA) have provided very valuable data to test our HRW model. As shown in the last section, the results from the present study demonstrate that the HRW model generally performs well for a total of 39 cases when compared to MADONA data. The results of our evaluation, on

the other hand, also indicate certain limitations in the HRW model applications. For example, the model may not simulate a gusty (unsteady) wind field as successfully as a steady wind field. Examination of these limitations and further testing of the model will allow us to gain insights consistent with the model physics and to develop a next generation model.

Finally, the results of a companion evaluation of the HRW model (Williamson et al. 2005) indicate that the correlation coefficient by itself is only a weak indicator of the model validity. In fact, that study showed that the HRW model performance for the MADONA field data is actually slightly worse than the homogeneous wind field used to initiate it, and this holds true for all statistical measures that were considered.

5. References

- Arya, S. P. *Air Pollution Meteorology and Dispersion*, Oxford University Press, 1999, 98–100.
- Ball, J. A.; Johnson, S. A. *Physically-based High-resolution Surface Wind and Temperature Analysis for EPAMS*; ASL-CR-78-0043-1; 1978, 270.
- Bradshaw, P. The Analogy Between Streamline Curvature and Buoyancy in Turbulent Shear Flow. *J. Fluid Mech.* **1969**, 36, Part 1, 177–191.
- Businger, J. A.; Wyngaard, J. C.; Izumi, Y.; Bradley, E. F. Flux Profile Relationships in the Atmospheric Boundary Layer. *J. Atmos. Sci.* **1971**, 28, 181–189.
- Caughey, S. J.; Wyngaard, J. C.; Kaimal, J. C. Turbulence in the Evolving Stable Boundary Layer. *J. Atmos. Sci.* **1979**, 36, 1041–1052.
- Cionco, R. M. On the Coupling of Canopy Flow to Ambient Flow for a Variety of Vegetation Types and Densities. *Boundary-Layer Meteorology* **1983**, 26, 325–335.
- Cionco, R. M. *Modeling Windfields and Surface Layer Profiles Over Complex Terrain and Within Vegetative Canopies, in the Forest-Atmosphere Interactions*; Eds. B. A. Hutchinson and B. B. Hicks, D. Reidel Publishing Company, 1985.
- Cionco, R. M. Windfield Simulations from a Hierarchy of Nested Meso- and Micrometeorological Models. *Proc. Sympo. Mesoscale Analysis & Forecasting*, Vancouver, Canada, 17–19 August 1987.
- Cionco, R. M.; Byers, J. H. Initialising the HRW Model with Meteorological Inputs from Different Scales to Optimize Model Output, Preprint Volume of the 11th Symposium on Boundary Layers and Turbulence, 27–31 March 1995, Charlotte, NC by the American Meteorological Society, Boston, MA, 1995.
- Cionco, R. M.; Byers, J. H. Influence of Airfield Structures and Complex Terrain upon Simulated Wind Fields, Preprint Volume of the 12th Symposium on Boundary Layers and Turbulence, 28 July–1 August 1997, Vancouver, BC Canada by American Meteorological Society, Boston MA, 1997.
- Cionco, R. M. Simulating Wind Fields for Different Resolutions of Terrain and Morphological Land Features, Second Urban Environment Symposium, 13th Conference on Biometeorology and Aerobiology, 2–6 November 1998, Albuquerque, New Mexico, American Meteorological Society, 1998.

- Cionco, R. M.; Weber, H.; aufm Kampe, W. High Resolution Meteorological Transport and Diffusion Simulations in a Complex river Valley, Preprint volume of the 23rd Conf. on Agricultural and Forest Meteorology, 13th conf. on Biometeorology and Aerobiology, and 2nd Urban Environment Symp., 2–6 November 1998, Albuquerque, NM, by AMS, Boston, MA, 1998.
- Cionco, R. M.; Ellefsen, R. High Resolution Urban Morphology Data for Urban Wind Flow Modeling. *Atmospheric Environment* **1998**, 32 (1), 7–17.
- Cionco, R. M.; et al. An Overview of MADONA: A Multinational Field Study of High-Resolution Meteorology and Diffusion over Complex Terrain. *Bulletin of the American Meteorological Society* **1999**, 80 (1), 5–19.
- Garratt, J. R. *The Atmospheric Boundary Layer*, Cambridge University Press, 1992, 316.
- Lanczos, C. *The Variational Principles of Mechanics (Third Edition)*, University of Toronto Press, 1966, 106–110.
- Lanicci, J. M., *Sensitivity Tests of a Surface-Layer Windflow Model to effects of stability and Vegetation*; AFGL-TR-85-0265; Air Force Geophysics Laboratory: Hanscom AFB, MA 01731, 1985.
- Orlanski, I. A rational Subdivision of Scales of Atmospheric Processes. *Bulletin of the Amer. Meteor. Soc.* **1975**, 56, 527–530.
- Panofsky, H. A.; Dutton, J. A. *Atmospheric Turbulence*; John Wiley & Sons, Inc. 1984; 397.
- Stull, R. B. *An Introduction to Boundary Layer Meteorology*; Kluwer Academic Publishers, 1988; 666.
- Tai, Chen-To. Generalized Vector and Dyadic Analysis. *IEEE Press* **1992**, 134.
- Thyckier-Nielsen S.; Mikkelsen, T.; Santabarbara, J.; Ride, D. J.; Higgs, T.; Weber, H. MADONA: Real-Time Diffusion Model Simulations, Preprint volume of the 11th Symp. on Boundary Layers and Turbulence, 27–31 March 1995, Charlotte, NC by AMS, Boston, MA, 1995.
- Wallace, J. M.; Hobbs, P. V. *Atmospheric Science, An Introductory Survey*; Academic Press, 1977; 467.
- Weber, H.; aufm Kampe, W.; Cionco, R. M. Visualization of the MADONA Data Base and Use of Selected Sequences in a Wind Flow and Diffusion Simulation System, Preprint volume of the 11th Symp. on Boundary Layers and Turbulence, 27–31 March 1995, Charlotte, NC, by AMS, Boston, MA, 1995.

Williamson, C. C.; Garvey, D. M.; Chang, S. S. *Revisiting the Analysis of the High Resolution Wind Model Using MADONA Field Data*; ARL-TR-3497; U.S. Army Research Laboratory: Adelphi, MD, 2005.

<u>No. of Copies</u>	<u>Organization</u>	<u>No. of Copies</u>	<u>Organization</u>
1 ELECT	ADMNSTR DEFNS TECHL INFO CTR ATTN DTIC OCP 8725 JOHN J KINGMAN RD STE 0944 FT BELVOIR VA 22060-6218	1	PM TIMS, PROFILER (MMS-P) AN/TMQ -52 ATTN B GRIFFIES BUILDING 563 FT MONMOUTH NJ 07703
1	CHAIRMAN JOINT CHIEFS OF STAFF ATTN J5 R&D DIV WASHINGTON DC 20301	1	US ARMY ENGRG DIV ATTN HNDED FD PO BOX 1500 HUNTSVILLE AL 35807
1	DARPA ATTN IXO S WELBY 3701 N FAIRFAX DR ARLINGTON VA 22203-1714	1	US ARMY INFO SYS ENGRG CMND ATTN AMSEL IE TD F JENIA FT HUACHUCA AZ 85613-5300
2	DIR OF DEFNS RSRCH & ENGRG ATTN DD TWP ATTN ENGRG WASHINGTON DC 20301	1	US ARMY MIS & SPC INTLLGNC CTR AIAMS YDL REDSTONE ARSENAL AL 35898-5500
1 CD	OFC OF THE SECY OF DEFNS ATTN ODDRE (R&AT) THE PENTAGON WASHINGTON DC 20301-3080	1	US ARMY NUC & CHEML AGCY 7150 HELLER LOOP STE 101 SPRINGFIELD VA 22150-3198
1	COMMANDING OFFICER ATTN NMCB23 6205 STUART RD STE 101 FT BELVOIR VA 22060-5275	1	COMMANDER US ARMY RDECOM ATTN AMSRD AMR W C MCCORKLE 5400 FOWLER RD REDSTONE ARSENAL AL 35898-5000
1	US ARMY RSRCH DEV AND ENGRG CMND ARMAMENT RSRCH DEV AND ENGRG CTR ARMAMENT ENGRG AND TECHNLGY CTR ATTN AMSRD AAR AEF T J MATTS BLDG 305 ABERDEEN PROVING GROUND MD 21005-5001	1	US ARMY STRTGC DEFNS CMND ATTN CSSD H MPL TECHL LIB PO BOX 1500 HUNTSVILLE AL 35807
1	DIR OF CHEM & NUC OPS DA DCSOPS ATTN TECHL LIB WASHINGTON DC 20301	1	CHIEF OF NAV OPS DEPT OF THE NAVY ATTN OP 03EG WASHINGTON DC 20350
1	NATL GROUND INTLLGNC CTR ATTN RSRCH & DATA BRANCH CHARLOTTESVILLE VA 22901-5396	1	US AIR FORCE TECH APPL CTR ATTN HQ AFTAC/TCC 1030 SOUTH HIGHWAY A1A PATRICK AFB FL 32925-3002
		1	CENTRAL INTLLGNC AGCY DIR DB STANDARD ATTN OSS/KPG/DHRT 1E15 OHB WASHINGTON DC 20505

<u>No. of Copies</u>	<u>Organization</u>	<u>No. of Copies</u>	<u>Organization</u>
1	US GOVERNMENT PRINT OFF DEPOSITORY RECEIVING SECTION ATTN MAIL STOP IDAD J TATE 732 NORTH CAPITOL ST NW WASHINGTON DC 20402	39	US ARMY RSRCH LAB ATTN AMSRD ARL CI E P CLARK ATTN AMSRD ARL CI ED C WILLIAMSON (5 COPIES) ATTN AMSRD ARL CI ED D GARVEY (5 COPIES) ATTN AMSRD ARL CI ED G D HUYNH (5 COPIES) ATTN AMSRD ARL CI ED S CHANG (20 COPIES) ATTN AMSRD ARL CI OK PE TECHL PUB ATTN AMSRD ARL CI OK TL TECH LIB ATTN IMNE ALC HRR MAIL & RECORDS MGMT ADELPHI MD 20783-1197
1	NATL CTR FOR ATMOS RSRCH ATTN NCAR LIBRARY SERIALS PO BOX 3000 BOULDER CO 80307-3000		
1	US ARMY RSRCH LAB ATTN AMSRD ARL CI OK TP TECH LIB T LANDFRIED BLDG 4600 ABERDEEN PROV 21005-5066		
1	DIRECTOR US ARMY RSRCH LAB ATTN AMSRD ARL RO EV W D BACH PO BOX 12211 RESEARCH TRIANGLE PARK NC 27709	TOTAL:	70 (68 HCs, 1 CD, 1 ELECT)
7	US ARMY RSRCH LAB ATTN AMSRD ARL CI ED D HOOCK (5 COPIES) ATTN AMSRD ARL CI D KNAPP (2 COPIES) BLDG 1622 WHITE SANDS MISSILE RANGE NM 88002-5501		

INTENTIONALLY LEFT BLANK